


Article

Study on Corrosion Resistance and Hydrogen Permeation Behavior in Inter-Critically Reheated Coarse-Grained Heat-Affected Zone of X80 Pipeline Steel

Kai Chen ^{1,2} , Wei Zhao ^{1,2,3,*}, Guangchun Xiao ^{1,2}, Ning Guo ^{1,2} and Hui Zhang ^{1,2,*}

¹ School of Mechanical Engineering, Qilu University of Technology (Shandong Academy of Sciences), Jinan 250353, China; cxk843217351@163.com (K.C.); xgc@qlu.edu.cn (G.X.); ningguo@qlu.edu.cn (N.G.)

² Shandong Institute of Mechanical Design and Research, Jinan 250031, China

³ School of Materials Science and Engineering, Tianjin University, Tianjin 300350, China

* Correspondence: zhaowei@qlu.edu.cn (W.Z.); zhanghui198787@163.com (H.Z.); Tel.: +86-135-8311-2741 (W.Z.); +86-135-8905-7218 (H.Z.)

Abstract: We studied the effects of peak temperature and cooling rate in the secondary welding thermal cycles on the martensite/austenite (M/A) constituents' characteristics (including fraction, average size and distribution), corrosion resistance and hydrogen permeation behaviors in the inter-critically reheated coarse-grained heat-affected zone (ICCGHAZ) of X80 pipeline steel. We observed that the M/A constituents' characteristics mainly depend on the secondary peak temperature and cooling rates, while the microstructure style and prior austenite grain size are dependent on the first peak temperature. In addition, the variations in the M/A constituents' characteristics result in different corrosion resistance and hydrogen permeation behaviors by changing the micro-galvanic effect and the number of hydrogen trapping sites. The high fraction and coarse grain size of M/A constituents are against the corrosion resistance and hydrogen permeation in ICCGHAZs, and their functional relationships are established. Moreover, the effects of the fraction of M/A constituents on the corrosion resistance and hydrogen permeation behaviors are much greater than those of the average size.

Keywords: inter-critically reheated coarse-grained heat-affected zone; M/A constituents; corrosion resistance; hydrogen permeation; X80 pipeline steel



Citation: Chen, K.; Zhao, W.; Xiao, G.; Guo, N.; Zhang, H. Study on Corrosion Resistance and Hydrogen Permeation Behavior in Inter-Critically Reheated Coarse-Grained Heat-Affected Zone of X80 Pipeline Steel. *Metals* **2022**, *12*, 1203. <https://doi.org/10.3390/met12071203>

Academic Editors: Alberto Moreira Jorge Junior and Amir Mostafaei

Received: 20 June 2022

Accepted: 13 July 2022

Published: 15 July 2022

Publisher's Note: MDPI stays neutral with regard to jurisdictional claims in published maps and institutional affiliations.



Copyright: © 2022 by the authors. Licensee MDPI, Basel, Switzerland. This article is an open access article distributed under the terms and conditions of the Creative Commons Attribution (CC BY) license (<https://creativecommons.org/licenses/by/4.0/>).

1. Introduction

In recent years, the development of offshore oil and gas resources has become the main growth point of the world energy industries. The increasing application of marine structural steels results in much stricter requirements for the welding of high-strength, low-alloyed steels, such as X80 pipeline steel. For the connection of thick steel plates, double-sided or multi-pass welding are unavoidable, indicating that some zones must undergo the secondary welding thermal cycles. Studies have shown that the heat-affected zone (HAZ) is usually a potential failure zone, especially the coarse-grained HAZ (CGHAZ) [1]. Therefore, research on the effects of secondary welding thermal cycles mainly focuses on its effects on the microstructure and properties of CGHAZ [2,3]. In the reheated CGHAZs, the severely coarse M/A constituents are formed in the inter-critically reheated CGHAZ (ICCGHAZ), whose secondary peak temperature is between A_{c1} and A_{c3} , resulting in the sharp decrease in toughness [4–6]. It has been found that the heat from extra weld pass may decrease the number of cracks, and may change their characteristics to improve the mechanical properties of the steel [7].

Localized corrosion has always been one of the important failure forms for pipeline steels, especially in welded joints [8–10]. Shi et al. [11] found that all HAZs except the fine-grained HAZ (FGHAZ) had worse corrosion resistance than the base metal in the CO_2

corrosion environments for X80 pipeline steels, which can be attributed to their coarse grains and the welding residual stress. Wang et al. [12] found that the CGHAZ and ICCGHAZ of X100 pipeline steel suffered a more severe corrosion than the base metal after immersion in the simulated alkaline soil solution, and a serious galvanic corrosion between the HAZ and the base metal can be introduced. In addition, it was found that the CGHAZ and ICCGHAZ of X100 pipeline steel suffered severe inter-granular corrosion in the simulated acidic soil solution due to their higher dislocation density and stronger corrosion reactivity, while the base metal mainly suffered uniform corrosion [13].

As a strong electrolyte, seawater is corrosive to metal materials [14]. Zhao et al. [15] studied the corrosion behavior in HAZ of FH32 steel in 3.5 wt% NaCl solution and found that the CGHAZ showed the worst corrosion resistance because the corrosion sensitivity of its microstructure is relatively high. In addition, the fraction, size and distribution of M/A constituents can affect the electrical resistance, and then further affect the corrosion resistance [16]. Nowadays, the cathodic protection, which can suppress anodic reactions, is widely used for marine metals in engineering [17]. However, the cathodic reactions are enhanced on the steel surface, resulting in the adsorbing, absorbing and diffusion of hydrogen atoms [18]. The concentration of hydrogen atoms inside the steel may further result in its hydrogen embrittlement fracture [19]. Studies have shown that the accumulation of hydrogen atoms and hydrogen embrittlement fracture are more prone to occur in welded joints, which can be attributed not only to the uneven hydrogen diffusion [20], but also to the appearance of M/A constituents that show susceptibility due to their local nanohardness [21]. Therefore, it is necessary to study the hydrogen permeation behaviors in HAZ and its mechanisms to explain the hydrogen-induced failure of pipeline steel welded joints. Xue et al. [22] and Liu et al. [23] found that the cementite (Fe_3C) in welded joints of X80 pipeline steel, as a kind of hydrogen trap, can hinder the diffusion of hydrogen in a certain way, and the smaller effective hydrogen diffusivity (D_{eff}) of HAZ can be attributed to the random distribution of Fe_3C . Zhao et al. [24] studied the effects of multiple welding thermal cycles on the hydrogen permeation parameters of X80 pipeline steel, and found that the D_{eff} was mainly determined by the peak temperature in the final welding thermal cycle. Deng et al. [25] studied the effects of reheated CGHAZ with different secondary peak temperatures and found that the hydrogen embrittlement susceptibility of ICCGHAZ with “necklace-like” M/A constituents was significantly increased.

However, most scholars tended to study the differences in corrosion resistance and hydrogen permeation between ICCGHAZ and other sub-zones of HAZ, and the effects of secondary peak temperature and cooling rates were ignored. In this research, the original CGHAZ and the ICCGHAZs with different secondary peak temperatures and cooling rates were obtained by welding thermal simulation technology. Potentiodynamic polarization curves, electrochemical impedance spectroscopy and electrochemical hydrogen permeation experiments were used to study their corrosion resistance and hydrogen permeation behaviors. We believe that the results of this research will provide a foundation for the uneven diffusion of hydrogen in welded joints.

2. Material and Experiment

2.1. Materials and Welding Thermal Simulation

The material used in this study is X80 pipeline steel, which is a low-carbon low-alloy steel. Its tensile strength is 779 MPa, yield strength is 560 MPa and elongation is 17.29%. Its chemical composition (wt%) is shown in Table 1. The empirical equations proposed to predict the austenite formation temperatures Ac_1 and Ac_3 for low-alloyed steel with less than 0.60 wt% C are as follows [26]:

$$\text{Ac}_1(^{\circ}\text{C}) = 723 - 10.7w(\text{Mn}) - 3.9w(\text{Ni}) + 29w(\text{Si}) + 16.7w(\text{Cr}) + 290w(\text{As}) + 6.38w(\text{W}) \quad (1)$$

$$\text{Ac}_3(^{\circ}\text{C}) = 910 - 230w(\text{C})^{0.5} - 15.2w(\text{Ni}) + 44.7w(\text{Si}) + 104w(\text{V}) + 31.5w(\text{Mo}) + 13.1w(\text{W}) \quad (2)$$

where w is the mass fraction of the element. It indicates that the microstructure begins to transform to austenite at 714 °C and has completely transformed to austenite at 879 °C.

Table 1. The chemical composition of X80 pipeline steel (wt%).

C	Si	Mn	Cr	Ni	Cu	Al	Ti	Mo	V	W	Pb	Sb	Zr	Nb	Fe
0.037	0.20	1.76	0.27	0.11	0.078	0.034	0.01	0.15	0.0033	0.033	0.0066	0.0021	0.013	0.07	Balance

In addition, the DSC test was carried out by NETZSCH DSC 404F3 (Selb, Germany). The results are shown in Figure 1. From the peaks of the DSC curve, it can be seen that the phase transition temperatures of X80 pipeline steel are 719 °C and 866 °C, indicating that the DSC test results are similar to the formula calculation results.

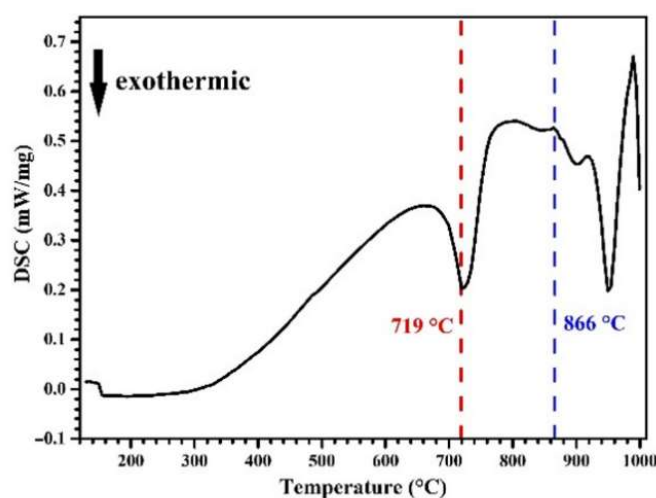


Figure 1. DSC test results of X80 pipeline steel.

The samples of X80 pipeline steel were machined to be rectangular with dimensions of 11 mm × 11 mm × 71 mm. Then, the welding thermal simulation experiments were carried out with the Gleeble-3500 thermomechanical simulator (Data Sciences International, New Brighton, MN, USA). The heating and cooling parameters (Table 2) were selected to simulate the microstructure of the original CGHAZ and different ICCGH AZs. The welding thermal cycle curves are shown in Figure 2. The different cooling rates were characterized by the cooling time $t_{8/5}$ (the time from 800 °C to 500 °C in the cooling process). No. 1–4 were to study the effect of different secondary peak temperatures on ICCGH AZ, and No. 3, 5 and 6 were to study the effect of different cooling rates on ICCGH AZ.

Table 2. Welding thermal simulation parameters.

No.	Name	Heating Rate (°C/s)	Holding Time at Peak (s)	First Thermal Cycle		Secondary Thermal Cycle	
				T_{p1} (°C)	$t_{8/5}$ (s)	T_{p2} (°C)	$t_{8/5}$ (s)
1	CGHAZ	160	1	1350	13.4	-	-
2	ICCGHAZ-1	160	1	1350	13.4	740	13.4
3	ICCGHAZ-2	160	1	1350	13.4	800	13.4
4	ICCGHAZ-3	160	1	1350	13.4	840	13.4
5	ICCGHAZ-4	160	1	1350	3	800	3
6	ICCGHAZ-5	160	1	1350	60	800	60

2.2. Microstructure Observations

The simulated CGHAZ and ICCGH AZs were polished step by step with 180–2000# metallographic sandpaper and diamond polishing agent with a particle size of 2.5 µm. The samples were etched with a suitable solution to reveal specific phases (The reagents used

in this paper were from Tianjin Kermel Chemical Reagent Co., LTD, Tianjin, China). One was 3% Nital (3 mL nitric acid and 97 mL ethanol) for the identification of microstructure, and the other was Le Pera (4 g picric acid in 100 mL ethanol, 1 g sodium metabisulfite in 100 mL deionized water; then the two solutions were mixed in a 1:1 ratio immediately before etching) for the specific identification of M/A constituents. The microstructure was characterized by a combination of KEYENCE VHX-5000 Optical Microscope (OM, Shenzhen senmeirui Technology Co., LTD, Shenzhen, China). According to the OM results, Image-Pro Plus 6.0 (Media Cybernetics, Rockville, MD, USA) was used to analyze the fraction and size of M/A constituents, and Nano Measurer 1.2 (Fudan University, Shanghai, China) was used to measure the size of prior austenite grains. The measurement of micro-hardness was carried out with the HXD-1000TMC micro-hardness tester (Xian Weixin Testing Equipment Co., LTD, Xi'an, China), in which the loading setting was 200 g and the loading time was 15 s. Each of the above experiments was repeated 10 times to ensure the accuracy and reproducibility of the results.

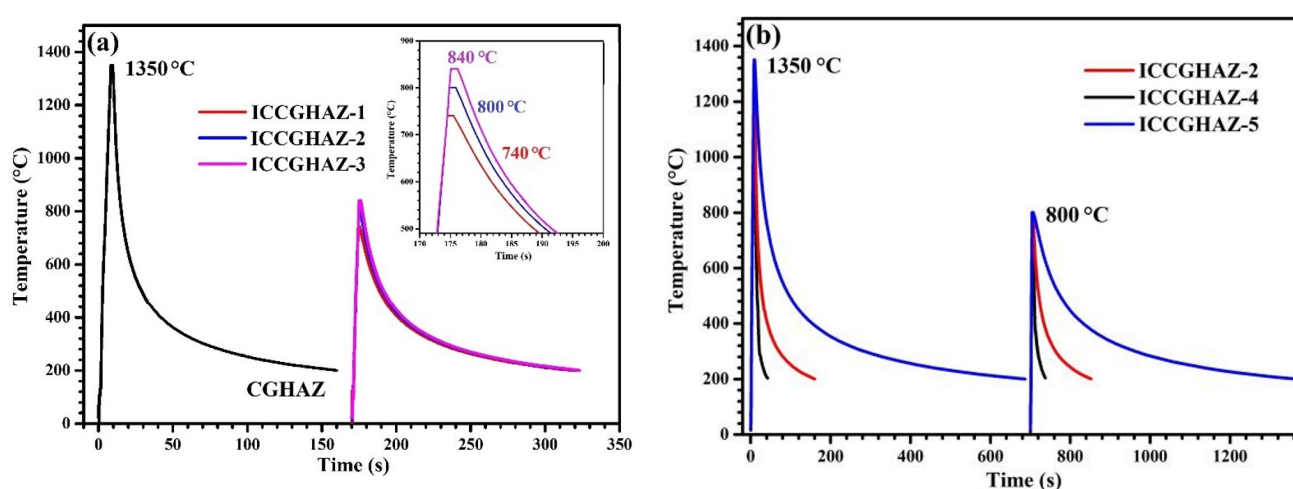


Figure 2. Schematic diagrams of the welding thermal cycles for different samples: (a) different secondary peak temperatures and (b) different cooling rates.

2.3. Electrochemical Tests

The electrochemical test solution was 3.5 wt% NaCl solution used to simulate the seawater environment, which was prepared from chemically pure reagents and ultrapure water. The electrochemical tests were performed on a GAMRY Interface 1010T electrochemical workstation (Gamry Instruments Consulting Co., LTD, Shanghai, China) at room temperature in a three-electrode battery. A sheet of platinum was used as the counter electrode, a saturated calomel electrode (SCE) was used as the reference electrode and the simulated CGHAZ and ICCGAZ samples were used as the working electrodes. The working electrodes were polished with 2000# metallographic sandpaper, rinsed with distilled water and ethanol, dried and sealed with insulating glue, leaving an exposed zone of 10 mm × 2 mm. OCP was recorded for 3600 s to reach a steady-state freely corroding condition; electrochemical impedance spectroscopy (EIS) measurements were performed with 10 mV amplitude and 0.01–100,000 Hz frequencies. The potentiodynamic polarization curves were measured from −1.2 to 1.2 V (vs. SCE) with a scanning rate of 0.5 mV/s. Each of the above experiments was repeated 3 times to ensure the accuracy and reproducibility of the results.

2.4. Hydrogen Permeation Test

According to the Devanathan–Stachurski double-cell method [27,28], the test adopted improved H-type double-electrolytic cells, and the sample was installed between the two cells with an exposed area of 0.385 cm² and a thickness of 1 mm. Before the experiment, a layer of nickel was plated on the surface of the sample in the hydrogen-detecting cell to

reduce the background current. A watt bath (250 g/L $\text{NiSO}_4 \cdot 6\text{H}_2\text{O}$, 45 g/L $\text{NiCl}_2 \cdot 6\text{H}_2\text{O}$, 40 g/L H_3BO_3) was used at room temperature at a current density of 5 mA/cm^2 and plating time of 5 min, rinsed with alcohol and dried after nickel plating. The hydrogen-charging cell was filled with 3.5 wt% NaCl + 1 g/L Na_2S solution, and a constant cathodic current density of 5 mA/cm^2 was applied. The hydrogen-detecting cell contained 0.2 mol/L NaOH solution, and anode passivation with an anodic potential of +200 mV (vs. SCE) was performed before hydrogen charging to eliminate background current. The hydrogen-charging current was provided by the DJS-292C potentiostat (Shanghai Xinrui Instrument Co., LTD, Shanghai, China), the anode potential was provided by the GAMRY Interface 1010T electrochemical workstation and the change in the hydrogen permeation current was recorded. Furthermore, the addition of Na_2S to the solution had little effect on the hydrogen permeation current, and as a poisoning agent, Na_2S prevented hydrogen atoms from recombining into hydrogen gas and increased the amount of hydrogen atoms diffusing into the sample, thereby improving the sensitivity of hydrogen permeation detection [29].

The steady-state hydrogen permeation flux J_∞ ($\text{mol} \cdot \text{cm}^{-2} \cdot \text{s}^{-1}$) was measured by the steady-state current density I_∞ ($\mu\text{A} \cdot \text{cm}^{-2}$). According to the following equation and results directly from Fick's first law, J_∞ was defined by [30]:

$$J_\infty L = \frac{I_\infty L}{nF} \quad (3)$$

where L (mm) is the thickness of samples, n is the number of transferred electrons ($n = 1$) and F is the Faraday constant ($F = 96,485 \text{ C} \cdot \text{mol}^{-1}$). The effective hydrogen diffusivity D_{eff} ($\text{cm}^2 \cdot \text{s}^{-1}$) can be calculated by [30]:

$$D_{\text{eff}} = \frac{L^2}{6t_L} \quad (4)$$

where t_L (s) is the time when the hydrogen permeation current is 63% of I_∞ . The adsorbed hydrogen concentration C_0 ($\text{mol} \cdot \text{cm}^{-3}$) can be calculated by [31]:

$$C_0 = \frac{J_\infty L}{D_{\text{eff}}} \quad (5)$$

In addition, the number of hydrogen trapping sites N_t (cm^{-3}) can be calculated by [32]:

$$N_t = \frac{nC_0}{3} \left(\frac{D_L}{D_{\text{eff}}} - 1 \right) \quad (6)$$

where n is the number of electrons transferred per mole ($n = 6.02 \times 10^{23} \text{ mol}^{-1}$), D_L is the lattice diffusion coefficient of hydrogen and the value in $\alpha\text{-Fe}$ is $1.28 \times 10^{-4} \text{ cm}^2 \cdot \text{s}^{-1}$.

3. Results

3.1. Microstructure and Micro-Hardness

3.1.1. Effect of the Secondary Peak Temperatures

The microstructure and M/A constituents of simulated CGHAZ and ICCGHAs with different secondary peak temperatures with the same $t_{8/5}$ of 13.4 s are shown in Figure 3, and the statistical fraction and average size of M/A constituents are shown in Figure 4; the error bars in the graphs are the standard deviation of all measurements corresponding to a point (same below). It can be seen that the microstructure of CGHAZ (Figure 3a) is mainly granular bainite, and its prior austenite grain size is about $36.65 \mu\text{m}$. The M/A constituents mainly distribute along the prior austenite grain boundaries and the granular bainite lath boundaries. They are parallel to each other in the same austenite grain, but their orientation is irrelevant in different austenite grains [16]. The fraction of M/A constituents is 4.35% and their average size is about $1.32 \mu\text{m}$.

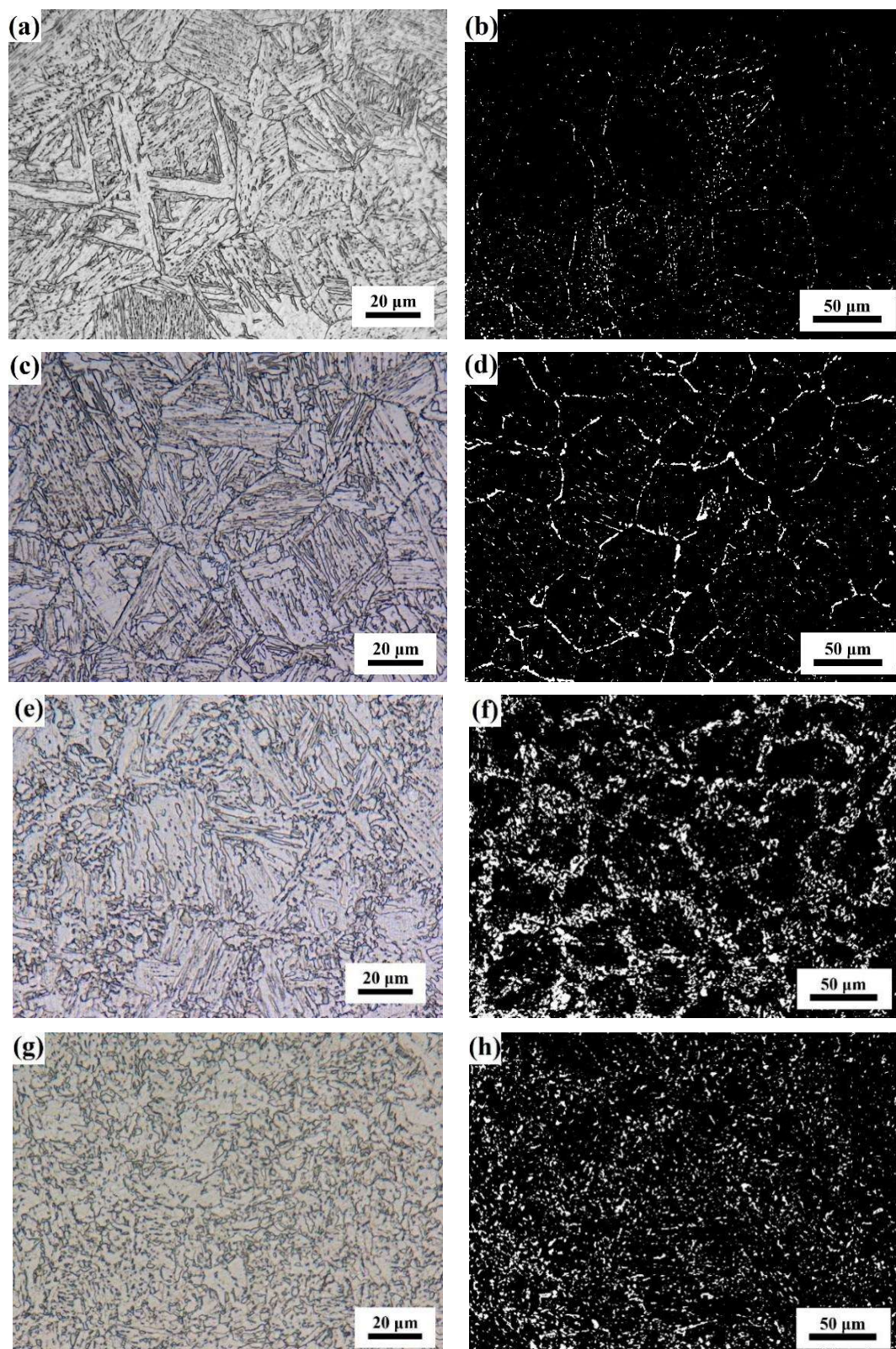


Figure 3. Microstructure and M/A constituents of the simulated CGHAZ and ICCGHAZs with different secondary peak temperatures: (a,b) CGHAZ; (c,d) ICCGHAZ-1; (e,f) ICCGHAZ-2; (g,h) ICCGHAZ-3.

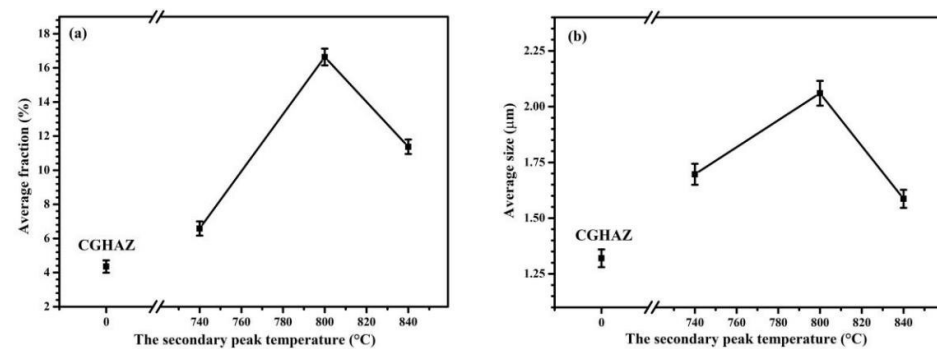


Figure 4. Fraction (a) and size (b) of M/A constituents in the simulated CGHAZ and ICCGHAZs with different secondary peak temperatures.

The microstructure of ICCGHAZ-1 (Figure 3c) and ICCGHAZ-2 (Figure 3e), whose secondary peak temperatures are 740 °C and 800 °C, respectively, is also mainly granular bainite, similar to that of CGHAZ. Their prior austenite grain size increases slightly to 38.29 and 39.33 μm, respectively. However, the characteristics of M/A constituents, including their fraction and average size, change greatly, although they also mainly embellish the prior austenite grain boundaries. For ICCGHAZ-1, the average size increases to 1.7 μm and the fraction increases to 6.58%, which are 28% and 51% more than those of CGHAZ, respectively. For ICCGHAZ-2, the M/A constituents are severely coarsened, showing a necklace-like shape with an average size of 2.06 μm, which is 56% bigger than that of CGHAZ. In addition, the fraction of M/A constituents is 16.64%, which is 3.8 times that of CGHAZ. The microstructure of ICCGHAZ-3 (Figure 3g), whose secondary peak temperature is 840 °C, is mainly granular bainite and polygonal ferrite, and the prior austenite grain boundaries disappear. The M/A constituents, with the average size of 1.59 μm, mainly present granular bainite showing uniform distribution. However, their fraction is still big, about 11.38%, which is 2.6 times that of CGHAZ.

As shown in Figure 5, the hardness of ICCGHAZs is higher than that of CGHAZ. With the increase in the secondary peak temperature, the hardness of ICCGHAZs first increases and then decreases, and the maximum value is reached at 800 °C.

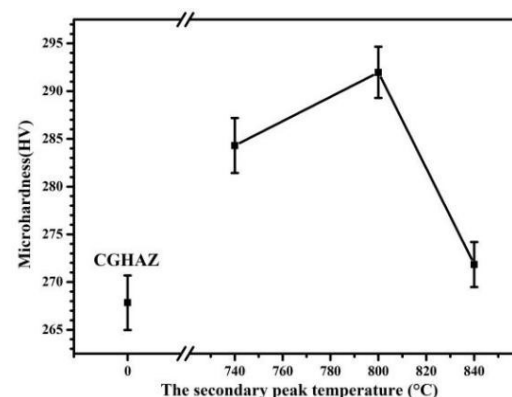


Figure 5. Micro-hardness of the simulated CGHAZ and ICCGHAZs with different secondary peak temperatures.

3.1.2. Effect of the Cooling Rates

The microstructure and M/A constituents of ICCGHAZs with different cooling rates with the same secondary peak temperature of 800 °C are shown in Figure 6, and the fraction and average size of M/A constituents are shown in Figure 7. It can be seen that the prior austenite grain boundaries are all visible and the microstructure is mainly granular bainite. Their prior austenite grain sizes are 39.82 and 38.52 μm, respectively, with a small difference from that of ICCGHAZ-2. Meanwhile, some bainitic ferrite appears in

the microstructure of ICCGHAZ-4 ($t_{8/5} = 3$ s), while the fraction of polygonal ferrite in the microstructure of ICCGHAZ-5 ($t_{8/5} = 60$ s) increases. More importantly, their M/A constituents' characteristics are different from ICCGHAZ-2. For ICCGHAZ-4, the M/A constituents, with an average size of $2.36 \mu\text{m}$ and fraction of 21.39%, also mainly distribute along the prior austenite grain boundaries presenting a necklace-like shape. However, for ICCGHAZ-5, the distribution of M/A constituents becomes more discrete, although there are some large-sized and sharp-angled M/A constituents embellishing the prior austenite grain boundaries. Its average size and fraction decrease to about $1.66 \mu\text{m}$ and 9.94%, respectively. It can be seen that the fraction and average size of M/A constituents gradually decrease as the cooling rate decreases (i.e., $t_{8/5}$ increases). In addition, the micro-hardness of ICCGHAZs gradually decreases with the decrease in cooling rates ($t_{8/5}$ increases), as shown in Figure 8.

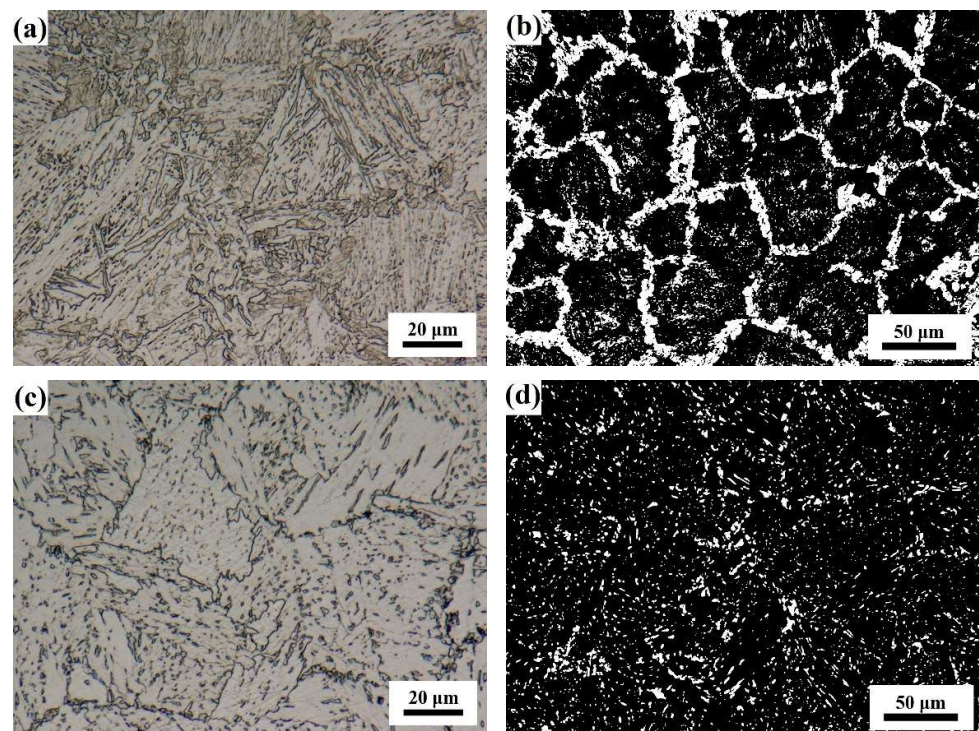


Figure 6. Microstructure and M/A constituents of the simulated ICCGHAZs with different cooling rates: (a,b) ICCGHAZ-4 and (c,d) ICCGHAZ-5.

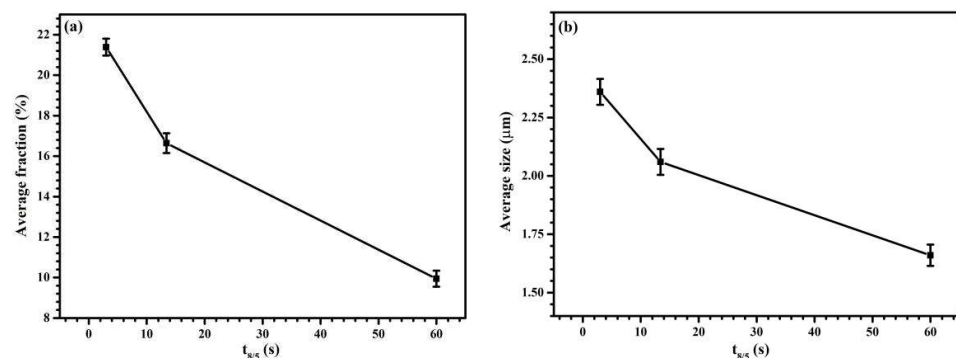


Figure 7. Fraction (a) and size (b) of M/A constituents in the simulated ICCGHAZs with different cooling rates.

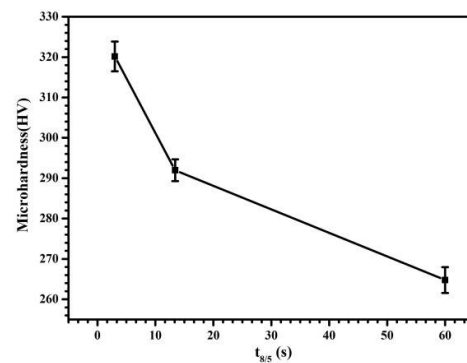


Figure 8. Micro-hardness of the simulated ICCGHAZs with different cooling rates.

3.2. Electrochemical Characteristics

3.2.1. Effect of the Secondary Peak Temperatures

Open Circuit Potential (OCP)

As shown in Figure 9, the open circuit potential (OCP) of simulated CGHAZ and ICCGHAZs with different secondary peak temperatures decrease and then keep stable as the immersion process develops. In addition, CGHAZ has the most positive OCP value, indicating that the corrosion driving force of CGHAZ is lower than that of ICCGHAZs. The OCP values of ICCGHAZs first decrease and then increase with the increase in the secondary peak temperature, and the most negative OCP value is reached at 800 °C.

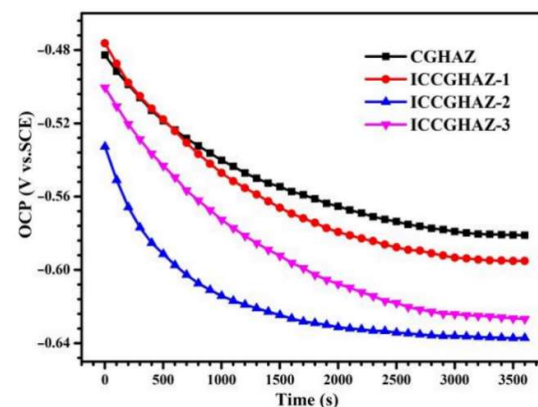


Figure 9. OCP dependent on the immersion time of the CGHAZ and ICCGHAZs with different secondary peak temperatures in 3.5 wt% NaCl solution.

Potentiodynamic Polarization Curves

The potentiodynamic polarization curves of simulated CGHAZ and ICCGHAZs with different secondary peak temperatures in 3.5 wt% NaCl solution are shown in Figure 10. The Tafel Curve Fitting method [33] is used to fit the corrosion potential (E_{corr}) and corrosion current density (i_{corr}) of different samples, and the results are presented in Figure 11. It can be seen that there is no passivation phenomenon for all samples, and the change rule of corrosion potential is consistent with that of OCP. The order of corrosion current density is CGHAZ < ICCGHAZ-1 < ICCGHAZ-3 < ICCGHAZ-2, indicating that the corrosion rates of ICCGHAZs are faster than that of CGHAZ, and the fastest corrosion rate is reached at the secondary peak temperature of 800 °C.

Electrochemical Impedance Spectroscopy (EIS)

As shown in Figure 12, all of the Nyquist impedance diagrams of simulated CGHAZ and ICCGHAZs contain capacitive reactance loops only in the first quadrant and have similar properties. The impedance film value gradually decreases as the frequency increases, and the phase angle reaches the maximum value when the frequency is about 1 Hz. The

equivalent circuit of $R_s(Q_{dl}R_{ct})$ is chosen to fit the EIS results, in which R_s is the solution resistance, Q_{dl} is the electric double-layer capacitance on the sample surface and R_{ct} is the charge transfer resistance. The fitting results of R_{ct} representing corrosion resistance are shown in Figure 13. It can be seen that the R_{ct} value of CGHAZ is greater than those of all ICCGHAZs. The R_{ct} values of ICCGHAZs first decrease and then increase with the increase in the secondary peak temperature, and the smallest R_{ct} value is reached at 800 °C. It can be seen that the results of EIS are consistent with the results of polarization curves.

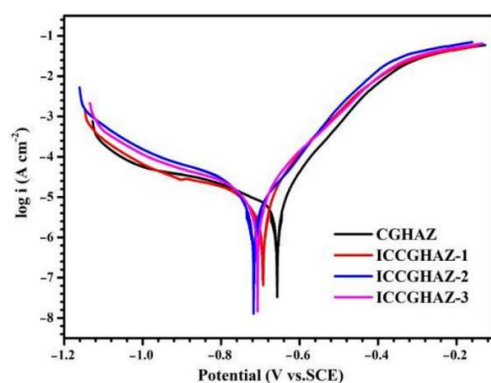


Figure 10. Potentiodynamic polarization curves of the CGHAZ and ICCGHAZs with different secondary peak temperatures in 3.5 wt% NaCl solution.

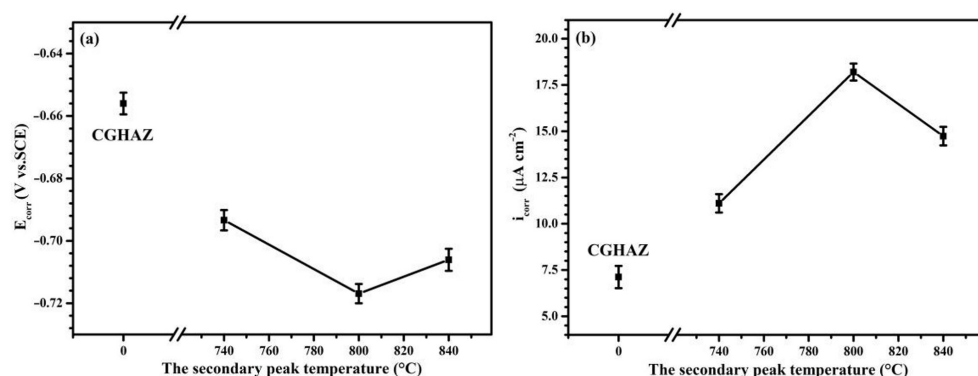


Figure 11. Fitting results of E_{corr} (a) and i_{corr} (b) for the CGHAZ and ICCGHAZs with different secondary peak temperatures in 3.5 wt% NaCl solution.

3.2.2. Effect of the Cooling Rates

Open Circuit Potential (OCP)

As shown in Figure 14, the OCP values of ICCGHAZs depend highly on the cooling rate. It can be seen that the corrosion driving force of ICCGHAZs decreases as the cooling rate decreases (i.e., $t_{8/5}$ increases).

Potentiodynamic Polarization Curves

The potentiodynamic polarization curves of simulated ICCGHAZs with different cooling rates in 3.5 wt% NaCl solution are shown in Figure 15, and the fitting results of E_{corr} and i_{corr} are shown in Figure 16. It can be seen that the corrosion potential results are consistent with OCP. In addition, the order of corrosion current density is $ICCGHAZ-5 < ICCGHAZ-2 < ICCGHAZ-4$, indicating that the corrosion rate of ICCGHAZs decreases as the cooling rate decreases (i.e., $t_{8/5}$ increases).

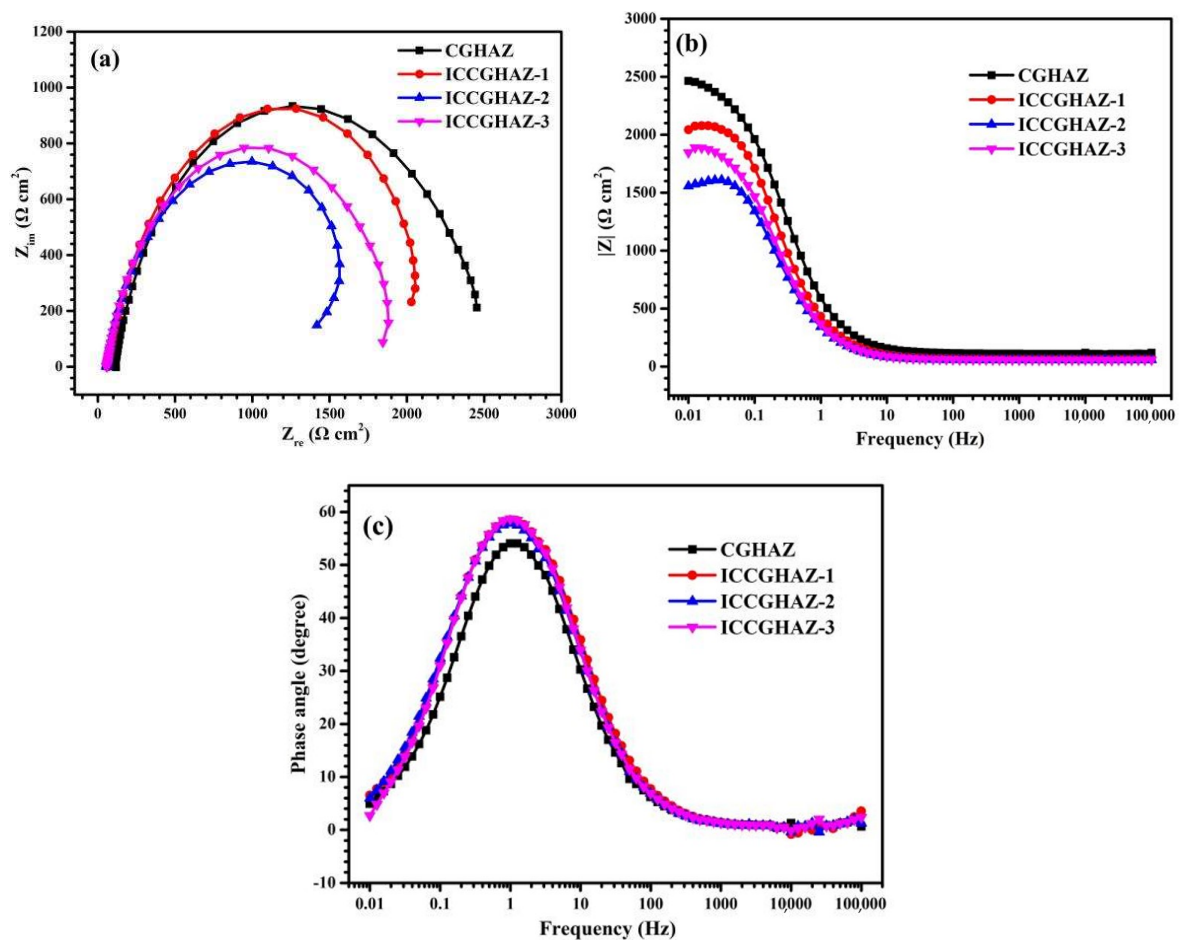


Figure 12. EIS results of the CGHAZ and ICCGHAZs with different secondary peak temperatures in 3.5 wt% NaCl solution: (a) Nyquist impedance diagrams, Bode diagrams of (b) impedance magnitude vs. frequency and (c) phase angle vs. frequency.

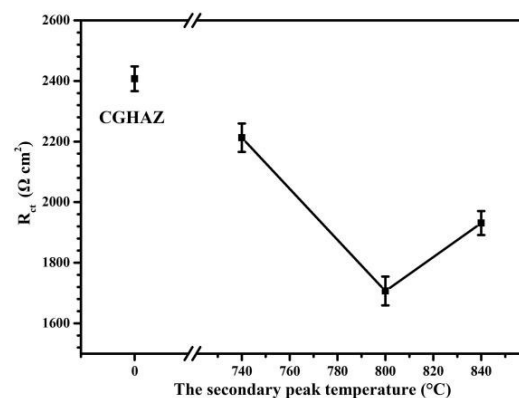


Figure 13. Fitting results of R_{ct} for the CGHAZ and ICCGHAZs with different secondary peak temperatures in 3.5 wt% NaCl solution.

Electrochemical Impedance Spectroscopy (EIS)

As shown in Figure 17, the Nyquist impedance diagrams of different ICCGHAZs are all capacitive reactance loops in the first quadrant with similar characteristics. The equivalent circuit of $R_s(Q_{dl}R_{ct})$ is chosen and the fitting results of R_{ct} are shown in Figure 18. It can be seen that the R_{ct} values of ICCGHAZs increase with the decrease in cooling rates ($t_{8/5}$ increase), which is consistent with the polarization curve results.

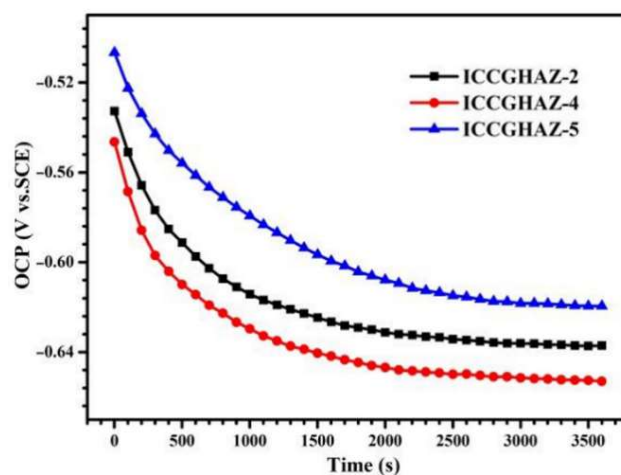


Figure 14. OCP dependent on the immersion time of the ICCGHAZs with different cooling rates in 3.5 wt% NaCl solution.

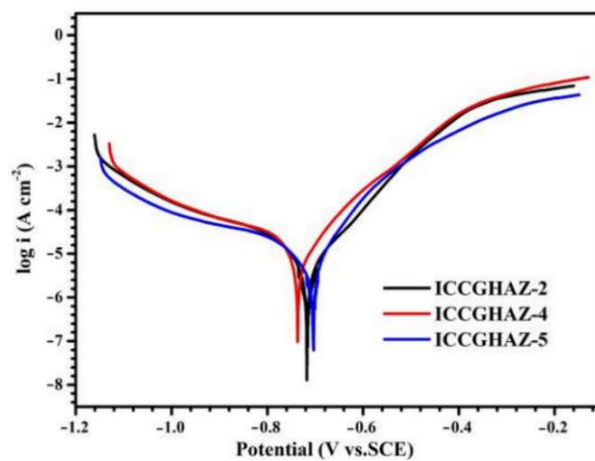


Figure 15. Potentiodynamic polarization curves of the ICCGHAZs with different cooling rates in 3.5 wt% NaCl solution.

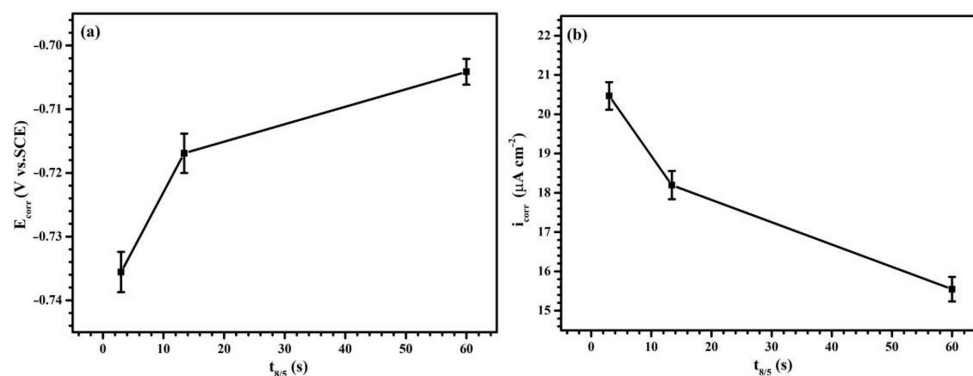


Figure 16. Fitting results of E_{corr} (a) and i_{corr} (b) for the ICCGHAZs with different cooling rates in 3.5 wt% NaCl solution.

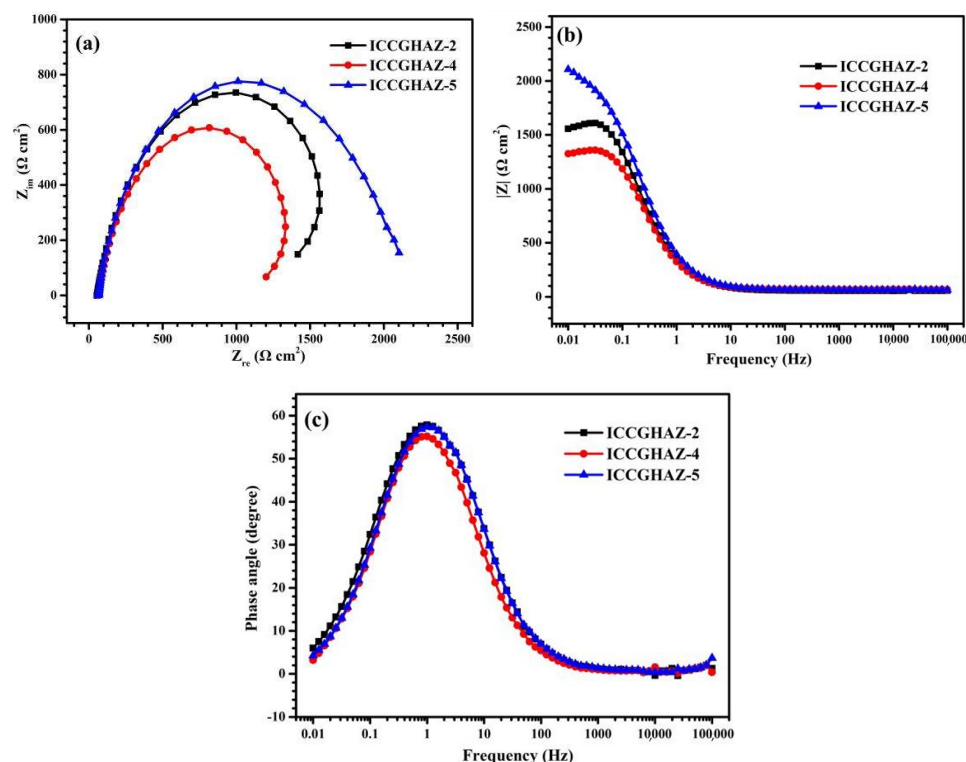


Figure 17. EIS results of the ICCGHAZs with different cooling rates in 3.5 wt% NaCl solution: (a) Nyquist impedance diagrams, Bode diagrams of (b) impedance magnitude vs. frequency and (c) phase angle vs. frequency.

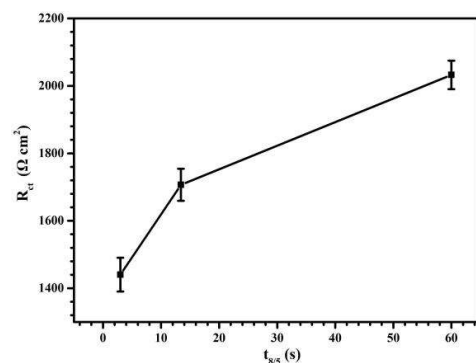


Figure 18. Fitting results of R_{ct} for the ICCGHAZs with different cooling rate in 3.5 wt% NaCl solution.

3.3. Hydrogen Permeation Behaviors

3.3.1. Effect of the Secondary Peak Temperatures

The hydrogen permeation curves of simulated CGHAZ and ICCGHAZs with different peak temperatures are shown in Figure 19. It can be seen that there is an incubation period of about 200 s for the increase in the hydrogen permeation current density, and then it increases to the steady state. According to Formulas (3)–(6), the effective hydrogen diffusivity (D_{eff}), the adsorbed hydrogen concentration (C_0) and the number of hydrogen trapping sites (N_t), which are commonly used to evaluate the hydrogen permeation behavior of materials, were obtained and are shown in Table 3. It can be seen that the D_{eff} value of CGHAZ is higher than those of all ICCGHAZs, while its C_0 and N_t values are lower. For ICCGHAZ, the D_{eff} value first decreases and then increases with the increase in the secondary peak temperature, while the C_0 values and N_t values are the opposite. The ICCGHAZ-2 has the smallest D_{eff} value and the largest C_0 value and N_t value. Generally, the hydrogen

embrittlement susceptibility of the pipeline steel is higher when the D_{eff} value is smaller, and the C_0 and N_t values are bigger [34]. Therefore, the order of hydrogen embrittlement susceptibility, i.e., the hydrogen-induced cracking susceptibility, of simulated CGHAZ and ICCGHAZs is CGHAZ < ICCGHAZ-1 < ICCGHAZ-3 < ICCGHAZ-2.

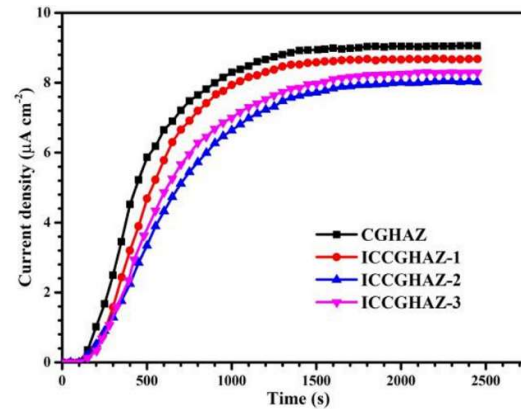


Figure 19. Hydrogen permeation curves of the CGHAZ and ICCGHAZs with different secondary peak temperatures.

Table 3. Hydrogen permeation parameters of the CGHAZ and ICCGHAZs with different secondary peak temperatures.

Sample	CGHAZ	ICCGHAZ-1	ICCGHAZ-2	ICCGHAZ-3
J_{∞} (10^{-11} mol·cm $^{-2}$ ·s $^{-1}$)	9.39	9.01	8.28	8.56
D_{eff} (10^{-6} cm 2 ·s $^{-1}$)	3.56	3.02	2.39	2.58
C_0 (10^{-6} mol·cm $^{-3}$)	2.64	2.97	3.46	3.32
N_t (10^{19} cm $^{-3}$)	1.85	2.47	3.65	3.24

3.3.2. Effect of the Cooling Rates

The hydrogen permeation curves of simulated ICCGHAZs with different cooling rates are shown in Figure 20, and the hydrogen permeation parameters of ICCGHAZs calculated by Formulas (3)–(6) are shown in Table 4. It can be seen that the D_{eff} values of ICCGHAZs increase, and the C_0 values and N_t values decrease as the cooling rate decreases ($t_{8/5}$ increases). Therefore, a higher cooling rate is beneficial to the increase in hydrogen embrittlement susceptibility.

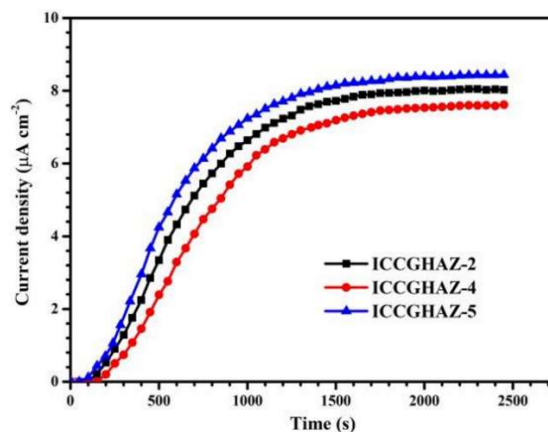


Figure 20. Hydrogen permeation curves of the ICCGHAZs with different cooling rates.

Table 4. Hydrogen permeation parameters of the ICCGHAZs with different cooling rates.

Sample	ICCGHAZ-2	ICCGHAZ-4	ICCGHAZ-5
J_{∞} (10^{-11} mol·cm $^{-2}$ ·s $^{-1}$)	8.28	7.90	8.75
D_{eff} (10^{-6} cm 2 ·s $^{-1}$)	2.39	2.07	2.77
C_0 (10^{-6} mol·cm $^{-3}$)	3.46	3.82	3.16
N_t (10^{19} cm $^{-3}$)	3.65	4.66	2.87

4. Discussion

4.1. Microstructure Evolution

It can be seen that the prior austenite grain size and the type of microstructure in ICCGHAZs mainly depend on the first peak temperature, which is in agreement with previous studies [35]. The prior austenite grain size in ICCGHAZs is slightly bigger than that in CGHAZ, which is mainly caused by the swallowing effect of the grains in the partial austenitization process. The coarsening of M/A constituents occurred in the secondary welding thermal cycle mainly because the secondary peak temperature is between Ac_1 and Ac_3 [36]. The prior austenite grain boundaries are the preferred location for austenite nucleation due to their high carbon content during the secondary welding thermal cycles in which the cooling time affects the diffusion of carbon atoms and the morphological changes of M/A constituents. According to the Arrhenius equation, the diffusion rate of carbon atoms can be calculated as follows [37]:

$$D = D_0 \exp\left(\frac{-Q}{RT}\right) \quad (7)$$

where D_0 is the initial diffusion rate of carbon atoms 6.2×10^{-7} m 2 ·s $^{-1}$, Q is the activation energy of carbon atom migration 80 kJ·mol $^{-1}$, R is the ideal gas state constant and T is the absolute temperature. Thus, carbon atoms' diffusion rates D can be calculated as 4.65×10^{-11} , 7.9×10^{-11} and 10.9×10^{-11} m 2 ·s $^{-1}$ at 740 °C, 800 °C and 840 °C, respectively. In addition, the carbon atoms' diffusion distance X_{3D} can be calculated as follows [37]:

$$X_{3D} = (6Dt)^{1/2} \quad (8)$$

where t is the time maintained at a certain temperature. In addition, the holding time at peak temperature for every sample in the secondary welding thermal cycles is 1 s, as shown in Table 2. Thus, carbon atoms' diffusion distance X_{3D} can be calculated as 16.7, 21.8 and 25.6 μ m for the ICCGHAZ samples with the secondary peak temperatures of 740 °C, 800 °C and 840 °C, respectively.

The X_{3D} of ICCGHAZ-2 is close to half of its prior austenite grain size, indicating that the carbon atoms have enough time to diffuse from the inside of the prior austenite grains to the boundaries. It results in a further increase in the carbon atom content of the prior austenite grain boundaries, and the carbon-rich supercooled austenite transforms into high-carbon martensite and incompletely transformed retained austenite in the next cooling process. The formed coarse M/A constituents are distributed in a necklace-like shape along the prior austenite grain boundaries with high carbon atom content. For ICCGHAZ-1, the formed M/A constituents are also distributed in a necklace-like shape along the prior austenite grain boundaries, but the fraction and size of M/A constituents are much smaller than those in ICCGHAZ-2, which is caused by the insufficient diffusion time of carbon atoms during the austenitization process. For ICCGHAZ-3 with the peak temperature close to Ac_3 , most of the original microstructure transformed into austenite in the heating process, resulting in the disappearance of the serious carbon-rich zone. In the subsequent cooling process, the supercooled austenite translates into polygonal ferrite and granular bainite, which makes M/A constituents with fine grain size and relatively low fraction. The higher micro-hardness of ICCGHAZs than CGHAZ can be attributed to the increased fraction of M/A constituents. ICCGHAZ-2 has the highest fraction of

M/A constituents, so its micro-hardness is also the highest. Although the fraction of M/A constituents in ICCGHAZ-3 is higher than that in ICCGHAZ-1, its micro-hardness is lower than that of ICCGHAZ-1 due to the existence of polygonal ferrite.

The X_{3D} of ICCGHAZ-4 and ICCGHAZ-5 is the same as that of ICCGHAZ-2, indicating that the diffusion time of carbon atoms for them is sufficient. For ICCGHAZ-4, the faster cooling rate results in the austenite transformation being relatively insufficient, and the high-temperature transformation products, such as ferrite, cannot be formed. At a low temperature, part of austenite transforms into high-carbon martensite and the others cannot transform due to the limitation of space. Therefore, a large number of M/A constituents with coarse grain size are formed in ICCGHAZ-4. For ICCGHAZ-5, the longer high temperature residence time results in the enlarging of the austenitization zone and the decline in the carbon atoms' segregation degree in the heating process results. In addition, the lower cooling rate results in the formation of ferrite at higher temperatures. Therefore, the fraction and size of M/A constituents decrease for ICCGHAZ-5.

4.2. Effect of M/A Constituents on Corrosion Behavior

All of the microstructures of CGHAZ and ICCGHAZs are mainly granular bainite. Therefore, the differences in corrosion behaviors for different samples can be attributed to the characteristics of M/A constituents, including their distribution, fraction and average size. The composition of M/A constituents, as the secondary phase, is different from that of the matrix microstructure (ferrite) in which the high-carbon martensite, with the high carbon content [38], has the ability to preferentially dissolve in the electrolyte [39]. The degree of its preferential dissolution mainly depends on the galvanic effect between the M/A constituents and their adjacent region. The corrosion resistance of ICCGHAZs is generally worse than that of CGHAZ, which can be attributed to its relatively strong galvanic effect due to the higher fraction, larger average size and higher carbon concentration of M/A constituents.

The i_{corr} and R_{ct} obtained by the electrochemical tests are usually used to represent the corrosion resistance. The binary linear regression fitting method is used to analyze the relationship between the $i_{\text{corr}}/R_{\text{ct}}$ and fraction and average size of M/A constituents for simulated CGHAZ and ICCGHAZs. The fitting results are shown in Figure 21; the Adj. R-Square of i_{corr} and R_{ct} are 0.84184 and 0.98404, respectively, indicating that the fitting results are in good agreement with the experimental results. The resulting formulas are as follows:

$$i_{\text{corr}} = 0.72931\alpha - 0.11696\beta + 6.19274 \quad (9)$$

$$R_{\text{ct}} = -55.50245\alpha + 18.53234\beta + 2572.27049 \quad (10)$$

where α is 100 times the fraction of M/A constituents, and β is the average size (μm) of M/A constituents. It can be seen that i_{corr} increases and R_{ct} decreases, indicating a decrease in corrosion resistance with the increase in fraction or average size of M/A constituents. As the fraction of M/A constituents increases, the number of micro-galvanic cells formed between the M/A constituents and the surrounding ferrite matrix increases, resulting in the decline in the corrosion resistance. In addition, the equations explain why the presence of the coarse necklace-like M/A constituents get along with the lower corrosion resistance. In addition, the absolute values of the coefficient for α in i_{corr} and R_{ct} are 6.24 and 3 times as much as those for β , indicating that the effect of the fraction of M/A constituents on corrosion resistance is much greater than that of average size.

4.3. Effect of M/A Constituents on Hydrogen Permeation Behaviors

The diffusion behavior of hydrogen in the metal materials is highly dependent on its phase or microstructure. For example, the D_{eff} value decreases sequentially for the microstructure of acicular ferrite, polygonal ferrite and martensite [24]. The different hydrogen diffusion behaviors of simulated CGHAZ and ICCGHAZs are attributed to the differences in their M/A constituents' characteristics. Studies show that the M/A con-

stituents, with different energy from the ferrite matrix, have high potential to be hydrogen trapping sites, hindering the diffusion of hydrogen [40].

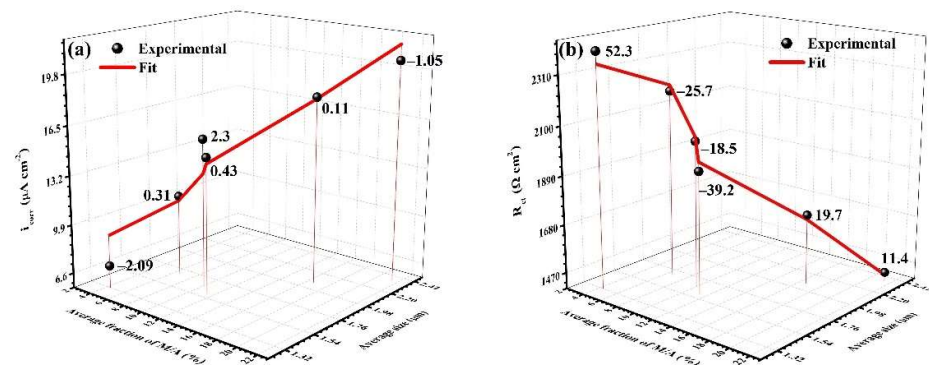


Figure 21. Fitting results of the functional relationship between i_{corr} (a), R_{ct} (b) and fraction of M/A constituents and average size.

The binary linear regression fitting method is also used to analyze the functional relationship between $D_{eff}/C_0/N_t$ and the fraction and average size of M/A constituents in CGHAZ and ICCGHAZs. As shown in Figure 22, the Adj. R-Square of D_{eff} , C_0 and N_t are 0.84038, 0.91819 and 0.95746, respectively, indicating that the fitting results are in good agreement with the experimental results. The obtained formulas are as follows:

$$D_{eff} = -7.91525 \times 10^{-8} \alpha + 2.51509 \times 10^{-8} \beta + 3.61408 \times 10^{-6} \quad (11)$$

$$C_0 = 6.43551 \times 10^{-8} \alpha - 3.26615 \times 10^{-8} \beta + 2.53263 \times 10^{-6} \quad (12)$$

$$N_t = 1.48023 \times 10^{18} \alpha + 6.81175 \times 10^{17} \beta + 1.2681 \times 10^{19} \quad (13)$$

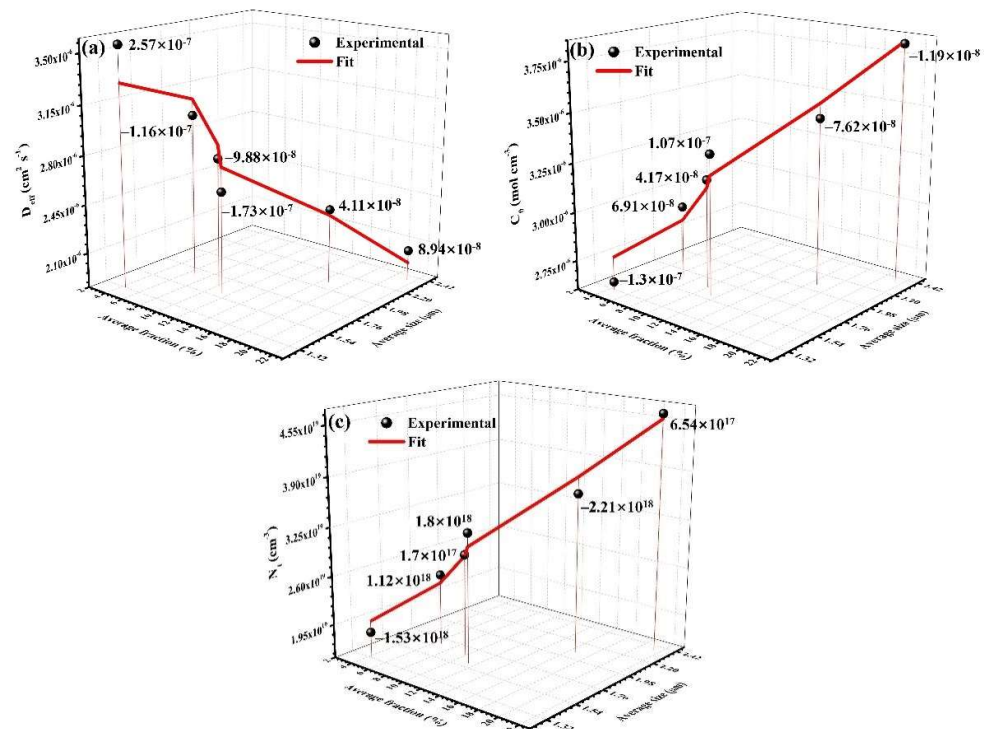


Figure 22. Fitting results of the functional relationship between D_{eff} (a), C_0 (b), N_t (c) and fraction of M/A constituents and average size.

It can be seen that D_{eff} decreases, while C_0 and N_t increase with the increase in the fraction of M/A constituents, indicating that the hydrogen permeation performance worsens. As the fraction of M/A constituents increases, the number of hydrogen capture sites, i.e., M/A constituents and their surrounding area, increases, resulting in an aggravation of the accumulation of residual hydrogen. In addition, it is indicated that the coarse M/A constituents, especially those showing a necklace-like shape, have high potential to be hydrogen trapping sites, resulting in the aggregation of hydrogen atoms. Therefore, high fraction and coarse grain size of M/A constituents are in favor of the hydrogen embrittlement and hydrogen-induced cracking. Moreover, the absolute values of the coefficient for α in the equations of D_{eff} , C_0 and N_t are about 3.15, 1.97 and 2.17 times as much as those for β , indicating that the effects of the fraction of M/A constituents on hydrogen permeation performance is much greater than that of the average size.

5. Conclusions

We investigated the microstructure evolution, corrosion resistance and hydrogen permeation behaviors for ICCGHAZs of X80 pipeline steels with different secondary peak temperatures and cooling rates. The main conclusions can be drawn as follows:

- (1) The fraction, average size and distribution of M/A constituents in ICCGHAZs depend highly on the secondary peak temperature and cooling rates, while their microstructure style and prior austenite grain size are dependent on the first peak temperature. In addition, lower cooling rates ($t_{8/5} = 3$ s) and a secondary peak temperature ($T_{p2} = 800$ °C) far away from Ac_1 and Ac_3 are beneficial to the formation of the “necklace-like” M/A constituents.
- (2) The differences in corrosion resistance and hydrogen permeation behavior of CGHAZ and ICCGHAZs are mainly caused by the variation in the M/A constituents’ characteristics, which can result in the increase in the micro-galvanic effect and the number of hydrogen trapping sites.
- (3) With the increase in the fraction and average size M/A constituents, the corrosion resistance and hydrogen permeability of ICCGHAZs gradually decrease. In addition, the fraction of M/A constituents has more influence on corrosion resistance and hydrogen permeation behaviors than their average size.

Author Contributions: Conceptualization, W.Z.; Data curation, K.C.; Formal analysis, K.C.; Funding acquisition, W.Z. and H.Z.; Investigation, K.C. and N.G.; Methodology, N.G.; Project administration, W.Z. and H.Z.; Resources, W.Z., G.X. and H.Z.; Supervision, W.Z., G.X. and H.Z.; Validation, K.C.; Visualization, K.C.; Writing—original draft, K.C.; Writing—review & editing, W.Z. All authors have read and agreed to the published version of the manuscript.

Funding: This work was supported by the National Nature Science Foundation of China (no. 51805285), the China Postdoctoral Science Foundation (2019M661016), the projects of Shandong Province “Youth innovation Science and Technology Support Plan” (2021KJ026), the Key Research and Development Project of Shandong Province (2021LYXZ014), the Innovation Team Project of Jinan (2019GXRC035) and the integration project of Science-Education-Industry of Qilu University of Technology (Shandong Academy of Sciences) [2022PY029].

Institutional Review Board Statement: Not applicable.

Informed Consent Statement: Not applicable.

Data Availability Statement: Not applicable.

Conflicts of Interest: The authors declare no conflict of interest.

References

1. Zhang, Y.; Xiao, J.; Liu, W.; Zhao, A. Effect of welding peak temperature on microstructure and impact toughness of heat-affected zone of Q690 high strength bridge steel. *Materials* **2021**, *14*, 2981. [[CrossRef](#)] [[PubMed](#)]
2. Arora, K.S.; Pandu, S.R.; Shajan, N.; Pathak, P.; Shome, M. Microstructure and impact toughness of reheated coarse grain heat affected zones of API X65 and API X80 linepipe steels. *Int. J. Press. Vessel. Pip.* **2018**, *163*, 36–44. [[CrossRef](#)]

3. Mohammadijoo, M.; Vallotton, J.; Collins, L.; Henein, H.; Ivey, D.G. Characterization of martensite-austenite constituents and micro-hardness in intercritical reheated and coarse-grained heat affected zones of API X70 HSLA steel. *Mater. Charact.* **2018**, *142*, 321–331. [\[CrossRef\]](#)
4. Wang, X.; Wang, Z.; Xie, Z.Y.; Ma, X.; Subramanian, S.; Shang, C.; Li, X.; Wang, J. Combined effect of M/A constituent and grain boundary on the impact toughness of CGHAZ and ICCGHAZ of E550 grade offshore engineering steel. *Math. Biosci. Eng.* **2019**, *16*, 7494–7509. [\[CrossRef\]](#) [\[PubMed\]](#)
5. Qi, X.; Di, H.; Wang, X.; Liu, Z.; Misra, R.; Huan, P.; Gao, Y. Effect of secondary peak temperature on microstructure and toughness in ICCGHAZ of laser-arc hybrid welded X100 pipeline steel joints. *J. Mater. Res. Technol.* **2020**, *9*, 7838–7849. [\[CrossRef\]](#)
6. Luo, X.; Chen, X.; Wang, T.; Pan, S.; Wang, Z. Effect of morphologies of martensite–austenite constituents on impact toughness in intercritically reheated coarse-grained heat-affected zone of HSLA steel. *Mater. Sci. Eng. A* **2018**, *710*, 192–199. [\[CrossRef\]](#)
7. Tomków, J.; Landowski, M.; Fydrych, D.; Rogalski, G. Underwater wet welding of S1300 ultra-high strength steel. *Mar. Struct.* **2022**, *81*, 103120. [\[CrossRef\]](#)
8. Du, X.; Dai, X.; Li, Z.; Du, X.; Shi, H.; Wu, J.; Lou, H.; Feng, X.; Zhao, L.; Li, Z. Corrosion analysis and anti-corrosion measures of oil casing of sulfur content gas wells: A case study of Daniudi gas field in the Ordos Basin. *Energy Rep.* **2021**, *7*, 1280–1292. [\[CrossRef\]](#)
9. Wang, Z.; Xie, F.; Wang, D.; Liu, J. Effect of applied potential on stress corrosion cracking behavior of X80 steel in alkaline soil simulated solution with sulfate-reducing bacteria. *Eng. Fail. Anal.* **2021**, *121*, 105109. [\[CrossRef\]](#)
10. Bordbar, S.; Alizadeh, M.; Hashemi, S.H. Effects of microstructure alteration on corrosion behavior of welded joint in API X70 pipeline steel. *Mater. Des.* **2013**, *45*, 597–604. [\[CrossRef\]](#)
11. Shi, C.; Zhang, Y.; Liu, P.; Xie, Y. Effects of second thermal cycles on microstructure and CO₂ corrosion behavior of X80 pipeline steel. *Int. J. Electrochem. Sci.* **2018**, *13*, 2412–2429. [\[CrossRef\]](#)
12. Wang, X.; Yang, Y.; Chen, Y.; Wang, H.; Wei, K. Corrosion behavior of X100 pipeline steel and its heat-affected zones in simulated alkaline soil solution. *Int. J. Electrochem. Sci.* **2019**, *14*, 9181–9192. [\[CrossRef\]](#)
13. Yang, Y.; Shi, X.; Sun, M.; Zeng, W. Corrosion behavior of X100 pipeline steel and its heat-affected zones in simulated acidic soil solution. *Int. J. Electrochem. Sci.* **2020**, *15*, 10994–11007. [\[CrossRef\]](#)
14. Shamir, M.; Junaid, M.; Khan, F.N.; Taimoor, A.A.; Baig, M.N. A comparative study of electrochemical corrosion behavior in Laser and TIG welded Ti–5Al–2.5Sn alloy. *J. Mater. Res. Technol.* **2019**, *8*, 87–98. [\[CrossRef\]](#)
15. Zhao, Z.P.; Xu, P.F.; Cheng, H.X.; Lu, X.Y.; Miao, J.; Chen, Y.; Yang, L. Investigation of influence of microstructure on FH32 steel corrosion properties using gleeble simulation of heat-affected zone and electrochemical methods. *Int. J. Electrochem. Sci.* **2019**, *14*, 9948–9959. [\[CrossRef\]](#)
16. Zhao, W.; Zou, Y.; Matsuda, K.; Zou, Z. Corrosion behavior of reheated CGHAZ of X80 pipeline steel in H₂S-containing environments. *Mater. Des.* **2016**, *99*, 44–56. [\[CrossRef\]](#)
17. Bell, A.M.; Von Der Au, M.; Regnery, J.; Schmid, M.; Meermann, B.; Reifferscheid, G.; Ternes, T.; Buchinger, S. Does galvanic cathodic protection by aluminum anodes impact marine organisms? *Environ. Earth Sci.* **2020**, *32*, 157. [\[CrossRef\]](#)
18. Li, X.; Ma, X.; Zhang, J.; Akiyama, E.; Wang, Y.; Song, X. Review of hydrogen embrittlement in metals: Hydrogen diffusion, hydrogen characterization, hydrogen embrittlement mechanism and prevention. *Acta Met. Sin. Engl.* **2020**, *33*, 759–773. [\[CrossRef\]](#)
19. Ramirez, M.F.G.; Hernández, J.W.C.; Ladino, D.H.; Masoumi, M.; Goldenstein, H. Effects of different cooling rates on the microstructure, crystallographic features, and hydrogen induced cracking of API X80 pipeline steel. *J. Mater. Res. Technol.* **2021**, *14*, 1848–1861. [\[CrossRef\]](#)
20. Zhao, W.; Zhang, T.; Zhao, Y.; Sun, J.; Wang, Y. Hydrogen permeation and embrittlement susceptibility of X80 welded joint under high-pressure coal gas environment. *Corros. Sci.* **2016**, *111*, 84–97. [\[CrossRef\]](#)
21. Castens, M.; Hoja, S.; Surm, H.; Hoffmann, F.; Fichte-Heinen, R.; Steinbacher, M. Hydrogen Absorption during Case Hardening of Steels EN20MnCr5 (SAE5120) and EN18CrNiMo7-6 (SAE4820). *Metals* **2022**, *12*, 6. [\[CrossRef\]](#)
22. Xue, H.; Cheng, Y. Hydrogen permeation and electrochemical corrosion behavior of the X80 pipeline steel weld. *J. Mater. Eng. Perform.* **2012**, *22*, 170–175. [\[CrossRef\]](#)
23. Liu, M.; Rivera-Díaz-del-Castillo, P.E.J.; Barraza-Fierro, J.I.; Castaneda, H.; Srivastava, A. Microstructural influence on hydrogen permeation and trapping in steels. *Mater. Des.* **2019**, *167*, 107605. [\[CrossRef\]](#)
24. Zhao, W.; Du, T.; Li, X.; Sun, H.; Li, B.; Yuan, S. Effects of multiple welding thermal cycles on hydrogen permeation parameters of X80 steel. *Corros. Sci.* **2021**, *192*, 109797. [\[CrossRef\]](#)
25. Deng, Q.; Zhao, W.; Jiang, W.; Zhang, T.; Li, T.; Zhao, Y. Hydrogen embrittlement susceptibility and safety control of reheated CGHAZ in X80 welded pipeline. *J. Mater. Eng. Perform.* **2018**, *27*, 1654–1663. [\[CrossRef\]](#)
26. Wang, L.; Liu, Z.; Cui, Z.; Du, C.; Wang, X.; Li, X. In situ corrosion characterization of simulated weld heat affected zone on API X80 pipeline steel. *Corros. Sci.* **2014**, *85*, 401–410. [\[CrossRef\]](#)
27. Huang, F.; Liu, J.; Deng, Z.; Cheng, J.; Lu, Z.; Li, X. Effect of microstructure and inclusions on hydrogen induced cracking susceptibility and hydrogen trapping efficiency of X120 pipeline steel. *Mater. Sci. Eng. A* **2010**, *527*, 6997–7001. [\[CrossRef\]](#)
28. Wang, D.; Xie, F.; Wu, M.; Sun, D.; Li, X.; Ju, J. The effect of sulfate-reducing bacteria on hydrogen permeation of X80 steel under cathodic protection potential. *Int. J. Hydrogen Energy* **2017**, *42*, 27206–27213. [\[CrossRef\]](#)
29. Haq, A.J.; Muzaka, K.; Dunne, D.P.; Calka, A.; Pereloma, E.V. Effect of microstructure and composition on hydrogen permeation in X70 pipeline steels. *Int. J. Hydrogen Energy* **2013**, *38*, 2544–2556. [\[CrossRef\]](#)

30. Han, Y.; Jing, H.; Xu, L. Welding heat input effect on the hydrogen permeation in the X80 steel welded joints. *Mater. Chem. Phys.* **2012**, *132*, 216–222. [[CrossRef](#)]
31. Wang, S.; Luu, W.; Ho, K.; Wu, J. Hydrogen permeation in a submerged arc weldment of TMCP steel. *Mater. Chem. Phys.* **2003**, *77*, 447–454. [[CrossRef](#)]
32. Xing, Y.; Yang, Z.; Yao, X.; Wang, X.; Lu, M.; Zhang, L.; Qiao, L. Comparative study on hydrogen induced cracking sensitivity of two commercial API 5L X80 steels. *Int. J. Press. Vessel. Pip.* **2022**, *196*, 104620. [[CrossRef](#)]
33. McCafferty, E. Validation of corrosion rates measured by the Tafel extrapolation method. *Corros. Sci.* **2005**, *47*, 3202–3215. [[CrossRef](#)]
34. Lin, J.; Chen, F.; Liu, F.; Xu, D.; Gao, J.; Tang, X. Hydrogen permeation behavior and hydrogen-induced defects in 316L stainless steels manufactured by additive manufacturing. *Mater. Chem. Phys.* **2020**, *250*, 123038. [[CrossRef](#)]
35. Li, X.; Fan, Y.; Ma, X.; Subramanian, S.V.; Shang, C. Influence of Martensite–Austenite constituents formed at different intercritical temperatures on toughness. *Mater. Des.* **2015**, *67*, 457–463. [[CrossRef](#)]
36. Li, X.; Shang, C.; Ma, X.; Subramanian, S.V.; Misra, R.D.K.; Sun, J. Structure and crystallography of martensite–austenite constituent in the intercritically reheated coarse-grained heat affected zone of a high strength pipeline steel. *Mater. Charact.* **2018**, *138*, 107–112. [[CrossRef](#)]
37. Li, X.; Ma, X.; Subramanian, S.V.; Shang, C.; Misra, R.D.K. Influence of prior austenite grain size on martensite–austenite constituent and toughness in the heat affected zone of 700MPa high strength linepipe steel. *Mater. Sci. Eng. A* **2014**, *616*, 141–147. [[CrossRef](#)]
38. Li, X.; Shang, C.; Ma, X.; Gault, B.; Subramanian, S.; Sun, J.; Misra, R. Elemental distribution in the martensite–austenite constituent in intercritically reheated coarse-grained heat-affected zone of a high-strength pipeline steel. *Scr. Mater.* **2017**, *139*, 67–70. [[CrossRef](#)]
39. Zhou, P.; Li, W.; Zhao, H.; Jin, X. Role of microstructure on electrochemical hydrogen permeation properties in advanced high strength steels. *Int. J. Hydrogen Energy* **2018**, *43*, 10905–10914. [[CrossRef](#)]
40. Izadi, H.; Tavakoli, M.; Moayed, M.H. Effect of thermomechanical processing on hydrogen permeation in API X70 pipeline steel. *Mater. Chem. Phys.* **2018**, *220*, 360–365. [[CrossRef](#)]